Pure Appl. Geophys. 169 (2012), 1443–1456

DOI 10.1007/s00024-011-0402-3

Pure and Applied Geophysics

An Elliptical Model for Deformation Due to Groundwater Fluctuations

Kristy F. Tiampo,[1] Francois-Alexis Ouegnin,[2,3] Sreeram Valluri,[2] Sergey Samsonov,[1] José Fernández,[4] and Garrett Kapp[1]

Abstract—Historically, surface subsidence as a result of subsurface groundwater fluctuations have produced important and, at times, catastrophic effects, whether natural or anthropogenic. Over the past 30 years, numerical and analytical techniques for the modeling of this surface deformation, based upon elastic and poroelastic theory, have been remarkably successful in predicting the magnitude of that deformation (Le Mouélic and Adragna in Geophys Res Lett 29:1853, 2002). In this work we have extended the formula for a circular-shaped aquifer (Geertsma in J Petroleum Tech 25:734–744, 1973) to a more realistic elliptical shape. We have improved the accuracy of the approximation by making use of the cross terms of the expansion for the elliptic coordinates in terms of the eccentricity, e, and the mean anomaly angle, M, widely used in astronomy. Results of a number of simulations, in terms of e and M developed from the transcendental Kepler equation, are encouraging, giving realistic values for the elliptical approximation of the vertical deformation due to groundwater change. Finally, we have applied the algorithm to modeling of groundwater in southern California.

Key words: Deformation, numerical techniques, groundwater hydrology, subsidence, inversion, geodesy.

1. Introduction

In many places today, anthropogenic surface deformation due to the evacuation of groundwater from underground aquifers presents a significant hazard to the surrounding communities and structures (Amelung *et al.*, 1999; Dixon *et al.*, 2006; Le Mouélic and Adragna, 2002; Tesauro *et al.*, 2000; Tomás *et al.*, 2005; Anderssohn *et al.*, 2008; Bell *et al.*, 2008; Motagh *et al.*, 2008). In addition, even in those areas where the potential damage is minimal, knowledge of the relationship between pumping rates and the associated subsidence can provide important information on the subsurface structure and nature of the associated aquifer.

Geertsma's (1973) pioneering work on the numerical modeling of land subsidence studied the causes of subsidence above hydrocarbon producing reservoirs. Here, a simple model was presented for the estimation of the reservoir compaction and the accompanying subsidence. This model is based on a mathematical formulation of the land subsidence above a disc-shaped oil and gas reservoir, and results in a circular approximation to the surface deformation caused by oil or groundwater pumping. The simplicity of this approach and its general applicability resulted in its widespread implementation.

In this paper we perform an expansion in terms of the eccentricity e and mean anomaly angle M of an ellipse in order to derive a second-order approximation to the ground deformation in an elliptic-shaped reservoir. We also exploit some interesting properties of the Bessel and Legendre special functions to find better estimates for that displacement.

Our work is organized as follows. First, we present a brief background discussion of the initial circular derivation and its application in Sect. 2. In the following Sect. 3 we present the derivation for the elliptical expansion and give examples of the induced deformation. We attempt to improve the estimates of the subsidence and their computation using a higher order approximation of the elliptic expansion. Section 4 demonstrates its applicability to the modeling of surface deformation due to groundwater fluctuations in southern California. Section 5 presents the conclusions.

[1] Department of Earth Sciences, University of Western Ontario, London, ON N6A-5B7, Canada. E-mail: ktiampo@uwo.ca
[2] Departments of Applied Math and Physics and Astronomy, University of Western Ontario, London, ON N6A 5B7, Canada.
[3] International University of Grand Bassam (IUGB), Grand Bassam, Côte d'Ivoire.
[4] Instituto de Geociencias (CSIC-UCM), Facultad de Ciencias Matemáticas, Ciudad Universitaria, Plaza de Ciencias 3, 28040 Madrid, Spain.

2. Initial Deformation Model

Geertsma (1973) invoked poroelasticity and thermoelasticity theory and assumed that both the reservoir and its surroundings were homogenous with respect to its compaction and permeability properties in order to derive an analytical formulation for the deformation induced by the removal of fluids from underground strata or reservoir. In that case, variables such as the uniaxial compaction coefficient, c_m, and the Poisson's ratio, v, remain fixed in an isotropic medium, and the derived surface deformation pattern is circular. The vertical (u_z) and radial (u_r) displacements at the surface ($z = 0$) then are obtained in terms of the product of two Bessel functions:

$$u_z(r,0) = -2c_m(1-v)\Delta pHR \int_0^\infty \mathrm{e}^{-D\alpha} J_1(\alpha R) J_0(\alpha r)\mathrm{d}\alpha \tag{1}$$

$$u_r(r,0) = +2c_m(1-v)\Delta pHR \int_0^\infty \mathrm{e}^{-D\alpha} J_1(\alpha R) J_1(\alpha r)\mathrm{d}\alpha \tag{2}$$

in which J_0 and J_1 are Bessel functions of the zero and first order, respectively, Δp is a uniform reservoir pressure reduction throughout the reservoir, H is the thickness of a disc-shaped reservoir, R is the radius of the reservoir, and D is the burial depth of that reservoir. Here z is positive in the up-direction; r is positive outward from the origin. The integration is performed over all possible nuclei of strain, α (Geertsma, 1973).

Note that, while Geertsma (1973) originally formulated his analysis in order to derive the subsidence induced by the pumping of oil from underground strata, the model can be applied to the pumping of groundwater from aquifers or, inversely, the injection of fluids into porous underground layers resulting in local uplift. Subsequent studies used a similar framework for the detection of ground deformation in a variety of regions. Applications can be found in the literature for cities such as Napoli, New Orleans, and Las Vegas (Amelung *et al.*, 1999; Dixon *et al.*, 2006; Tesauro *et al.*, 2000).

In a recent study of the city of Paris, France, Le Mouélic and Adragna (2002) investigated surface uplift due to the infiltration of groundwater in the area of the Saint Lazare Railway. They used a remote sensing technique, interferometric synthetic aperture radar (InSAR) (Massonnet and Feigl, 1998) to identify the displacement, and the analytical model above (Geertsma, 1973), to estimate the ground deformation. They concluded that the groundwater deformation that occurred could be modeled successfully using this approach, and consisted of an elastic reversible deformation.

The main objective of this model is to describe the land subsidence due to the modification of the pressure in an underlying circular reservoir. Here, again, it is assumed that the medium is uniform and isotropic, such that the permeability in all directions is a constant. Le Mouélic and Adragna (2002) defined the following simple framework: an elastic earth treated as an elastic half-space with a Poisson ratio v, a disc-shaped reservoir of radius R and thickness h, buried at a depth D, and a groundwater height variation due to the pressure drop that is denoted dh. The vertical displacement of the surface $u_z(r)$ depends on the radial distance r, where the origin above the center of the reservoir is determined by the location of the pumping or injection operation.

The formula for the displacement is then:

$$u_z(r) = +(2v-2)dhR \int_0^\infty \mathrm{e}^{-D\alpha} J_1(\alpha R) J_0(\alpha r)\mathrm{d}\alpha \tag{3}$$

$$u_r(r) = -(2v-2)dhR \int_0^\infty \mathrm{e}^{-D\alpha} J_1(\alpha R) J_1(\alpha r)\mathrm{d}\alpha \tag{4}$$

here dh is linked to the reservoir thickness H, and the increase of pressure Δp by the relation $dh = c_m H\Delta p = \frac{H\Delta p}{E}$ (Landau and Lifshitz, 1986; Le Mouélic and Adragna, 2002).

3. Elliptical Approximation

In natural underground aquifers, the medium rarely is isotropic. While variations can occur on many scales, the predominant case seen in nature is

where there are differing permeabilities, or hydraulic conductivity, in two different, primarily orthogonal directions, so that permeability varies with azimuthal direction (Burbey, 2006; Freeze and Cherry, 1979; Kim, 2005). This anisotropy can be caused by differences in directional porosity that are a result of grain size variations, depositional environment, fracture patterns, and pressure. This causes a slower rate of groundwater evacuation in one direction than the other, and a smaller total amount of extraction in that direction and a shorter distance over which that extraction occurs. The result is an elliptical shape for the surface height change, as seen from above. Here we attempt to provide a better approximation to the actual deformation seen in nature through the derivation of a formula for surface deformation that varies elliptically with the angle of rotation of the radius r around the center of the aquifer. This formula is obtained via a mathematical approximation of the transcendental Kepler equation that has been used to relate the eccentric anomaly angle E in terms of the mean anomaly M and the orbital eccentricity e for planetary motion and other astronomical applications.

In order to obtain an accurate elliptical orbit that relates the orbital eccentricity e and the mean anomaly angle M to the eccentric anomaly E, Valluri *et al.* (2006) introduced the following modifications to the Cartesian coordinates x and y of a circular orbital motion,

$$x = a(\cos E - e) \tag{5}$$

$$y = a\left(\sqrt{1-e^2}\right)\sin E \tag{6}$$

$$E \approx M + \left(e - \frac{e^3}{8}\right)\sin M + \frac{1}{2}e^2 \sin 2M + \frac{3}{8}e^3 \sin 3M + \mathrm{O}(e^4) \tag{7}$$

where E and M are the eccentric and mean anomaly angles widely used in astronomy and astronautics, etc., x and y are the Cartesian coordinates that describe the motion of the stellar object, and a and e stand for the radius of the circular orbit and the eccentricity of the elliptical orbit.

Equation (7) is obtained from an iterative method of the transcendental Kepler equation:

$$E_{i+1} = M + e\sin E_i, \quad i = 0, 1, 2\ldots \tag{8}$$

The trigonometric formulae for $\sin(A+B)$ and the series expansion of $\sin x$ and $\cos x$ for small x are also used (Murray and Dermott, 1999). The final series for $E - M$ is in fact a Fourier sine series in the mean anomaly M, with the coefficients of the series $C_S(e)$ of the form:

$$C_S(e) = \frac{2}{s}J_s(se), \quad s = 1, 2, 3, \cdots \tag{9}$$

where $J_s(se)$ is the Bessel function with running index s and argument se.

It is of interest to note that a more generic analysis of the Kepler equation displays the connection of the singularities in the complex M plane to those of the eccentricity e (Hagihara, 1970). The singularities are obtained by the solution in terms of the Lambert W function. The Lambert W function has seen a renaissance not only among physicists and mathematicians but also researchers in many diverse fields during recent years (Corless *et al.*, 1996). This function has shown its ubiquity in innumerable applications. Also of special interest for this present paper is the application of the Lambert W function for the calculation of wave water heights due to refraction and friction (Valluri *et al.*, 2000) and the movement of water in the soil from the Richards equation in hydrology (Barry *et al.*, 1993). The application of the Lambert W function and the Lambert hyperfunction in connection with the transcendental Kepler equation and the curves of Hippias (Corless *et al.*, 1996) warrants a separate study in its own right.

Different levels of accuracy can be obtained by taking into consideration the cross terms that result from the expression for the radial coordinate r in terms of x and y. We choose, for brevity, to study only two cases, the case without the cross terms, which we call the zero order accuracy approximation, and the case with the cross terms included, which we designate as the higher order accuracy approximation.

3.1. Zero Order Accuracy Approximation

We insert the series for E in Eq. (7), above, into the formulas for x and y in Eqs. (5) and (6), and omit the cross terms in the trigonometric functions to obtain a zero-order approximation of the following form:

$$x = -\frac{3ae}{2} + a\left(1 - \frac{3e^2}{8}\right)\cos(M) + \frac{1}{2}ae\cos(2M) + \frac{3}{8}ae^2\cos(3M) \quad (10)$$

$$y = a\left(1 - \frac{3e^2}{8}\right)\sin(M) - \frac{1}{4}ae^2\sin(M) + \frac{1}{2}ae\sin(2M) + \frac{3}{8}ae^2\sin(3M). \quad (11)$$

The formulae in Eqs. (10) and (11) take into account the eccentricity and the mean anomaly. New radii $r(e)$ and $R(e)$ can be defined to approximate the elliptic shape taking the eccentricity into consideration. After simplification, each new radius has the following approximate form:

$$r(e) = \left\{a^2\left(1 - \frac{3}{8}e^2\right)\left[1 + \frac{160\,e^2 + (20 - 2\cos 2M)e^4}{\left(1 - \frac{3}{8}e^2\right)}\right]\right\}^{\frac{1}{2}} \quad (12)$$

The eccentricity is chosen to be greater than 0 and less than 1 in order to arrive at an ellipse, whereas the angle remains between $-\pi$ and π. The description of the eccentric and mean anomaly and their computation can be found in Logsdon (1997). Therefore, the formula of the vertical displacement becomes

$$u_{ze}(r_e) = +(2v - 2)dhR_e \int_0^\infty \mathrm{e}^{-D\alpha}J_1(\alpha R_e)J_0(\alpha r_e)\mathrm{d}\alpha \quad (13)$$

$$u_{re}(r_e) = -(2v - 2)dhR_e \int_0^\infty \mathrm{e}^{-D\alpha}J_1(\alpha R_e)J_1(\alpha r_e)\mathrm{d}\alpha \quad (14)$$

where u_e, r_e, and R_e are a function of the eccentricity, e.

Here we have not revised the original analytical computation for the deformation, based upon elasticity theory. We have approximated the variation in shape resulting from bidirectional variations in the hydraulic conductivity, or permeability, via a modification to the allowable spatial extent of the deformation that is controlled by the extent of the anisotropy in the permeability. In Fig. 1 we plot the results for this approximation for the vertical deformation $u_{ze}(r_e)$ for the case in which $e = 0$, or the circular case, again using the values $H = 23$ m, $D = 25$ m, $v = 0.3$, $dh = 1.01$ cm, and $R = 400$ m. The contour shown is coincident with the upper corner value at the aquifer edge. Note that these results are identical to those of the circular formulation given in Eq. (3).

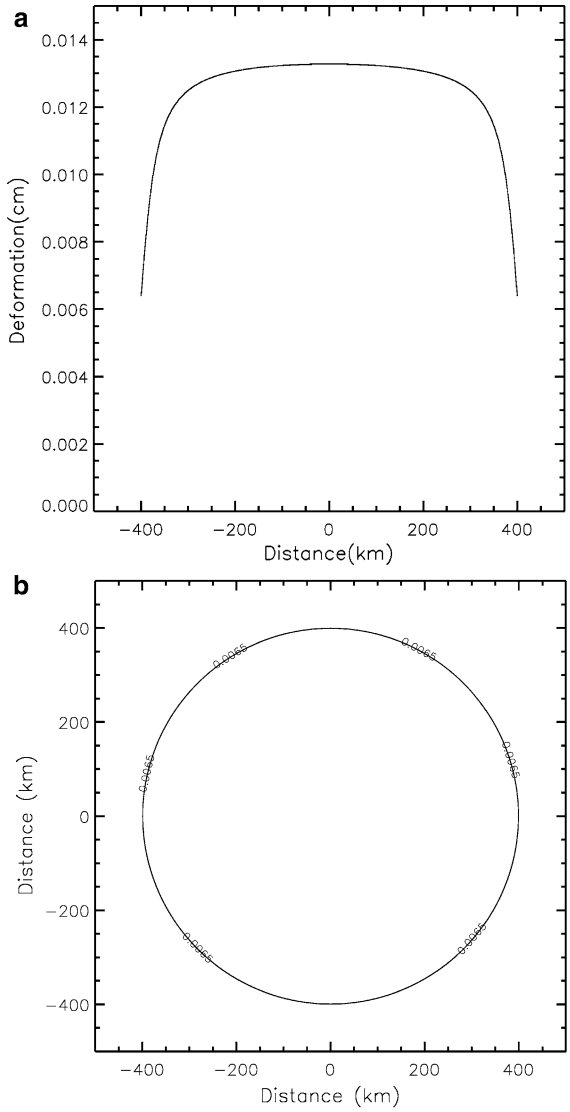

Figure 1
Results for change in surface height, $u_z(r)$, for $H = 23$ m, $D = 25$ m, $v = 0.3$, $dh = 1.01$ cm, and $R = 400$ m, for a circular aquifer, using the elliptical approximation of Eq. 13 (*solid line*). **a** Shows a cross section across the centerline of the aquifer, while **b** shows the map view along the outside edge of the aquifer. Note that these results are indistinguishable from those of Eq. 3 (Le Mouélic and Adragna, 2002)

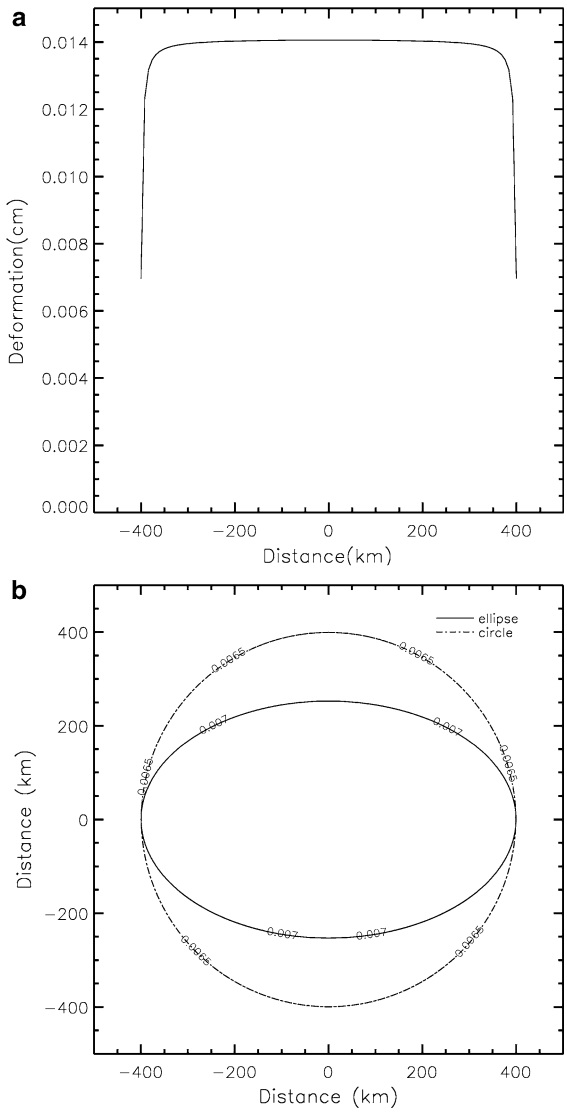

Figure 2
Results for change in surface height, $u_z(r_e)$, for $H = 23$ m, $D = 25$ m, $\nu = 0.3$, $dh = 1.01$ cm, and $R = 400$ m, for an aquifer with eccentricity = 0.6, using the elliptical approximation of Eq. 13 (*solid line*). **a** and **b** are the same as for Fig. 1 above. Included in **b**, for reference, is the circular approximation of Eq. 3 (*dashed line*)

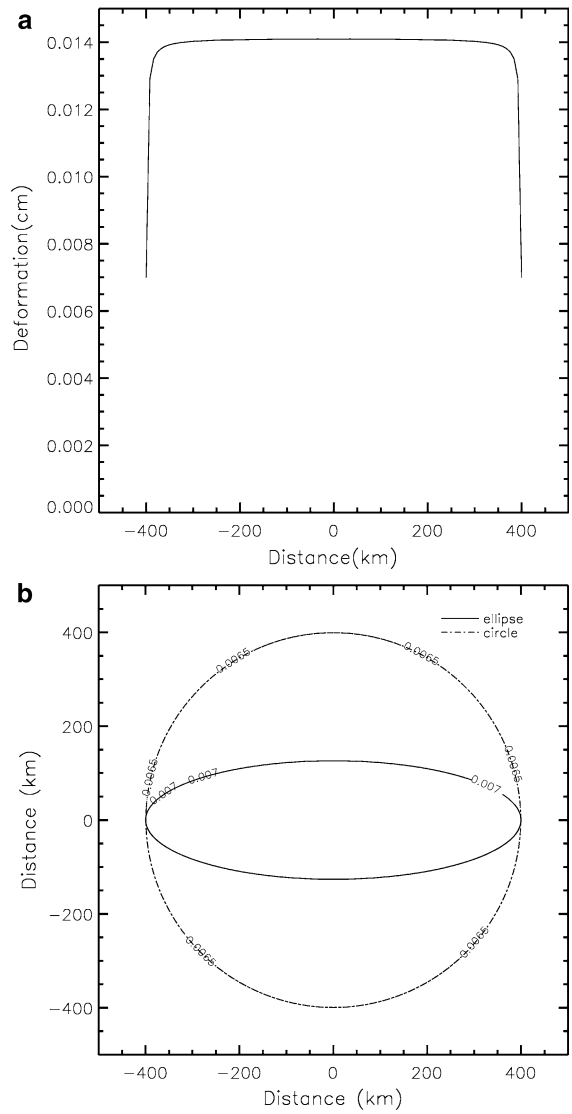

Figure 3
Results for change in surface height, $u_z(r_e)$, for $H = 23$ m, $D = 25$ m, $\nu = 0.3$, $dh = 1.01$ cm, and $R = 400$ m, for an aquifer with eccentricity = 0.9, using the elliptical approximation of Eq. 13 (*solid line*). **a** and **b** are the same as for Fig. 1 above. Included in **b**, for reference, is the circular approximation of Eq. 3 (*dashed line*)

As additional examples, we focus on two cases where the eccentricity differs from zero. We chose the values 0.6 and 0.9 and we provide their plots in Figs. 2 and 3, respectively. Included with each is the circular approximation for comparison.

Figure 4 shows a cross section of the vertical deformation along the long axis of the elliptical aquifer, using the zero order approximation of Eq. (13). Note that the maximum values of the estimates from our elliptical approximation increase gradually with increasing eccentricity, and that the edges of the profiles become sharper and steeper as well.

3.2. Higher Order Accuracy Approximation

A higher order accuracy approximation for $r_h(e)$ can be obtained by including the cross terms of the corrections presented in (Valluri *et al.*, 2006). The following expression is obtained using the properties of Bessel functions and their associated integrals (Gradshteyn and Ryzhik, 1965; Wang and Guo, 1989):

$$r_h(e) = \left\{ a^2\left(1 - \frac{3}{8}e^2 + \left(2 + \frac{13}{32}e^2\right)e^2\right) \times \left[1 + \frac{e^2\left(\cos(M)\left(\frac{e^2-2}{e}\right) - e\cos(3M)\right) + e^4\left(-\cos(2M)\left(\frac{1+e^2}{2e^2}\right) + \frac{3\cos(4M)}{32}\right)}{\left(1 - \frac{3}{8}e^2 + \left(2 + \frac{13}{32}e^2\right)e^2\right)}\right]\right\}^{\frac{1}{2}} \quad (15)$$

where $r_h(e)$ is the new radius, M is the mean anomaly as above, and a and e again are the radius of the circular orbit and the eccentricity. Again, the new radii $r_h(e)$ and $R_h(e)$ can be defined to approximate the elliptic shape, using Eq. (15). The new equations for deformation are then

$$u_{zh}(r_h) = +(2v-2)dhR_h \int_0^\infty \mathrm{e}^{-D\alpha} J_1(\alpha R_h) J_0(\alpha r_h)\mathrm{d}\alpha \quad (16)$$

$$u_{rh}(r_h) = -(2v-2)dhR_h \int_0^\infty \mathrm{e}^{-D\alpha} J_1(\alpha R_h) J_1(\alpha r_h)\mathrm{d}\alpha. \quad (17)$$

The higher order approximation of Eq. (16) is calculated for varying radii and the parameters used in Sect. 3.1, above. As before, Fig. 5 shows the calculated vertical deformation for an eccentricity of 0.6, and Fig. 6 shows the same calculation for an eccentricity of 0.9.

Figure 7 is a cross section of the vertical deformation across the long axis of the aquifier, for varying eccentricities and the higher order approximation of Eq. (16). Note that there are significant differences between the vertical displacement derived with the higher order approximation and the zero order approximation shown in Fig. 4. The zero order approximation had a more square shape, as noted above, while we observe a more bell-shape when we add the cross terms in the higher order approximation. The second point to remark is that the maximum value of the vertical deformation does not increase uniformly with increasing ellipticity, so that the deformation is not accommodated by a uniform volumetric increase.

4. Modeling Groundwater Deformation in Southern California

4.1. Background

The northern region of southern California's Los Angeles basin is bounded to the north by the San Gabriel Mountains and the Puente Hills and Montebello Hills to the south. This area, known as the San Gabriel Valley (Fig. 8), has a significant compressional tectonic strain component oriented approximately north–south. However, accurate estimation of the amplitude of the tectonic rate of strain has been difficult due to contamination from other geophysical sources, particularly anthropogenic signals associated with groundwater pumping in the region (Argus and Gordon, 2001; Bawden *et al.*, 2001; Watson *et al.*, 2002; Lanari *et al.*, 2004; Argus *et al.*, 2005; King *et al.*, 2007).

Dense population and rapid industrial development make this southern California a prime location for geodetic studies of earthquake hazard. However, the most rapid movements in this region are non-tectonic deformations due to groundwater and oil extraction. For example, the 40-km-long Santa Ana basin subsides at the steady rate of 12 mm/year with the seasonal fluctuation of 55 mm in the vertical direction and 7 mm in the horizontal direction

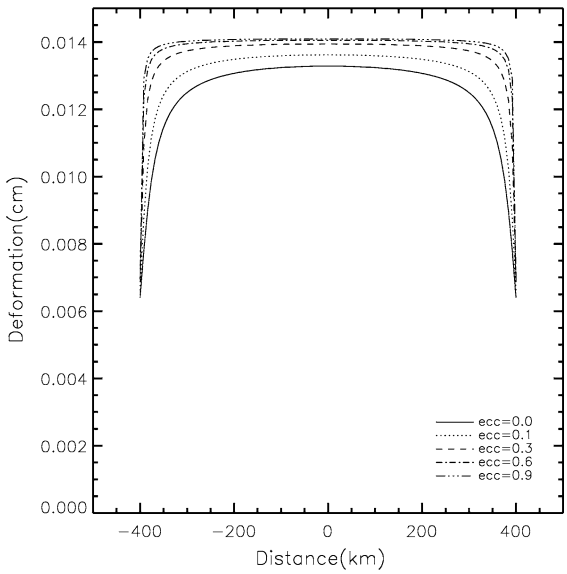

Figure 4
Cross section of the change in surface height, $u_z(r_e)$, through the long axis of the aquifer for varying eccentricity using the elliptical approximation of Eq. 13. As above, $H = 23$ m, $D = 25$ m, $v = 0.3$, $dh = 1.01$ cm, and $R = 400$ m

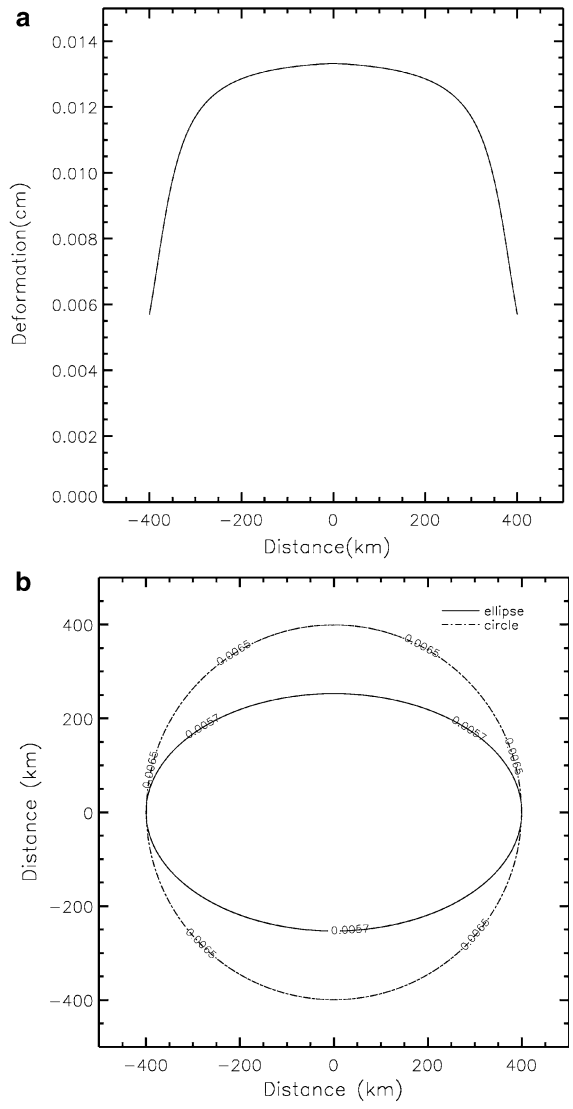

Figure 5
Results for change in surface height, $u_z(r_h)$, for $H = 23$ m, $D = 25$ m, $v = 0.3$, $dh = 1.01$ cm, and $R = 400$ m, for an aquifer with eccentricity $= 0.6$, using the elliptical approximation of Eq. 16 (*solid line*). **a** and **b** are the same as for Fig. 1 above. Included in **b**, for reference, is the circular approximation of Eq. 3 (*dashed line*)

[Watson *et al.*, 2002]. The horizontal movement is governed mostly by plate tectonics ranging from 1.8 cm/year (south) to 0.9 cm/year (north) in N–S direction and from −4 cm/year (southwest) to −3.2 (northeast) in the E–W direction. However, Bawden *et al.* (2001) estimated that after removing anthropogenic signals the uniaxial contraction across the Los Angeles basin can be observed at a rate of 0.44 cm/year in the northeast direction perpendicular to the major strike-slip faults in this area. Argus *et al.* (2005) estimated anthropogenic horizontal velocities to be more than 1 mm/year at more than 1/3 of the GPS stations in the region, and shortening (contraction) to the south of the San Gabriel mountains at 4.5 ± 1 mm/year.

4.2. Data

From previous investigations, it is evident that differential interferograms carry significant amounts of useful data in the studies of phenomena such as surface deformations due to seismic events (Jacobs *et al.*, 2002; Massonnet *et al.*, 1993, Massonnet and Feigl, 1998) and volcanic activities (Fernández *et al.*, 2005), mining subsidence (Gourmelen *et al.*, 2007) or groundwater extraction (Schmidt and Bürgmann, 2003; Bawden *et al.*, 2001, Watson *et al.* 2002). Different types of errors are also present in the interferograms and these need to be estimated and, if possible, corrected.

Recently, Samsonov *et al.* (2007) computed three-dimensional surface velocity maps for that part of

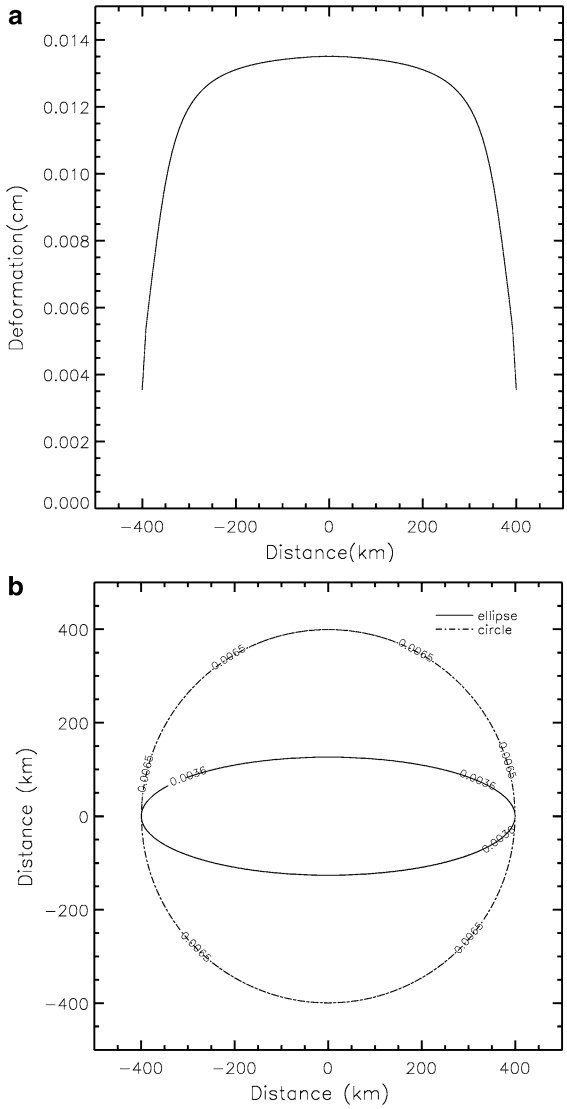

Figure 6
Results for change in surface height, $u_z(r_e)$, for $H = 23$ m, $D = 25$ m, $v = 0.3$, $dh = 1.01$ cm, and $R = 400$ m, for an aquifer with eccentricity = 0.9, using the elliptical approximation of Eq. 16 (*solid line*). **a** and **b** are the same as for Fig. 1 above. Included in **b**, for reference, is the circular approximation of Eq. 3 (*dashed line*)

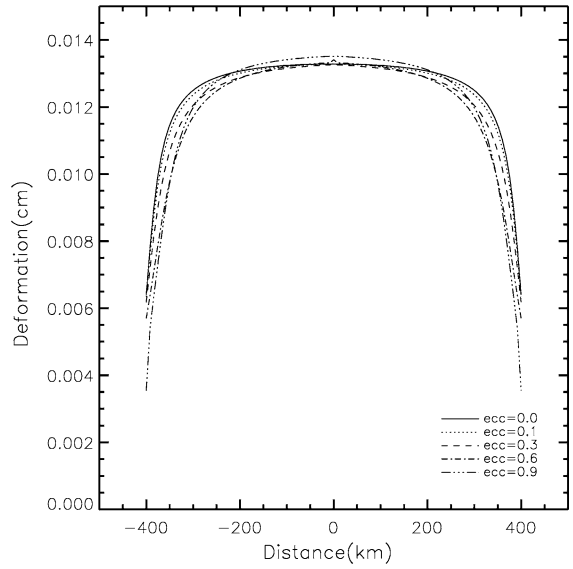

Figure 7
Cross section of the change in surface height, $u_z(r_e)$, through the long axis of the aquifer for varying eccentricity using the elliptical approximation of Eq. 16. As above, $H = 23$ m, $D = 25$ m, $v = 0.3$, $dh = 1.01$ cm, and $R = 400$ m

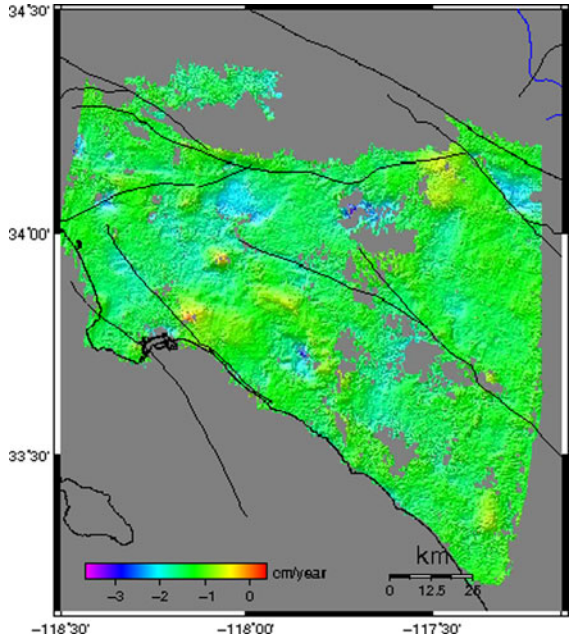

Figure 8
DInSAR interferogram, ERS2 September 2, 2000 to October 23, 2003

southern California between the Los Angeles basin and the San Gabriel Mountains. They developed a method based on random field theory within a Bayesian statistical framework to derive three-dimensional surface motion maps from sparse GPS measurements and differential interferometric synthetic aperture radar (DInSAR) interferograms in the southern California region. In this method, minimization of the Gibbs energy function is performed analytically (Samsonov and Tiampo, 2006). The problem is well posed and the solution is unique

and stable and not biased by the continuity condition. The technique produces a three-dimensional field containing estimates of surface motion on the spatial scale of the DInSAR image, over a given time period, complete with error estimates. Significant improvement in the accuracy of the vertical component and moderate improvement in the accuracy of the horizontal components of velocity are achieved in comparison with the GPS data alone.

In this work we used the DInSAR interferogram shown in Fig. 8 with a time span of 2.97 year (02 September 2000—23 August 2003). This interferogram was processed from ERS-2 level 0 (raw data) using the JPL/Caltech Repeat Orbit Interferometry Package (*ROI PAC*, version 2.3) (Rosen *et al.*, 2004). To reduce water vapour effects on the interferogram, the GPS/MODIS integrated water vapour correction model demonstrated in (Li *et al.*, 2005) was applied. This processing involved the usual steps of image coregistration, interferogram computation, baseline estimation from Delft precise orbits and interferogram flattening and removal of topographic phase by using a 30 m SRTM DEM. At this stage, a Zenith Path Delay Difference Map (ZPDDM) derived from GPS-calibrated MODIS near IR water vapour fields was inserted into the interferometric processing sequence, followed by phase unwrapping and baseline refinement. In order to obtain the unwrapped water vapor corrected interferogram, a new simulated interferogram was created using the refined baseline and topography, and was subtracted from the unwrapped phase (including orbital ramp) with the water vapor model removed (Li *et al.*, 2005). Since InSAR has no absolute reference datum, the unwrapped phase has been shifted by the mean difference between InSAR and GPS range changes when compared to GPS-derived range changes in the LOS direction.

The GPS-DInSAR integration was performed using preprocessed time series from 140 GPS stations from the Southern California integrated GPS network Southern California Integrated GPS Network (SGICN) (Hudnut *et al.*, 2002). This data was reprocessed in order to remove outliers and offsets. Three components (north, east and up) of the velocity vector then were calculated by applying linear regression to the time span of the differential interferogram. Finally, ordinary kriging is used in order to interpolate GPS data at the intermediate locations.

The GPS-DInSAR optimization results are shown in Fig. 9. The appearance of the northern image practically does not change due to the orientation of the satellite in the current coordinate system. The eastern component of the velocity, however, has more significant changes, especially in the southern part. The strong velocity gradient in both the north and east components is visible, which suggests that this analysis can be used to improve the accuracy of the estimation of shortening across the Los Angeles basin. The vertical component shows the combination of signals from both GPS and DInSAR measurements. A few areas are of particular interest. A strong uplift with the approximate velocity of 0.6–0.8 cm/year is observed in the southern part of the Los Angeles basin (34.8N, −118.2E), due to seasonal changes and/or rebound in the local groundwater levels. A few areas of subsidence are presented in the northern part of the image. The middle region (around 34N, −117.6E) is the rapid subsidence which is presented on many other interferograms starting from the mid-1990s (Watson *et al.*, 2002). The top right subsidence (34.1N, −117.2E) that is originally presented only on the DInSAR interferogram is amplified on the final image and contours the fault. It is the groundwater uplift signal seen at −118.3, 33.8 that we will attempt to model here.

4.3. Inversion

The velocity change seen in Fig. 9 was converted to deformation over a smaller region centered on the vertical component of the groundwater deformation noted above, displayed in Fig. 10. Figure 10 shows the net deformation over this time period of almost 3 years, with the plate velocities removed. Deformation is shown in the east (Fig. 10a), north (Fig. 10b) and up (Fig. 10c) directions. While the vertical deformation is clearly defined, with a pseudo-elliptical shape, and a maximum deformation of approximately 4 cm, the deformation in the east and north direction is significantly smaller (note the difference in scale). However, there is some deformation above the background, particularly in the east component.

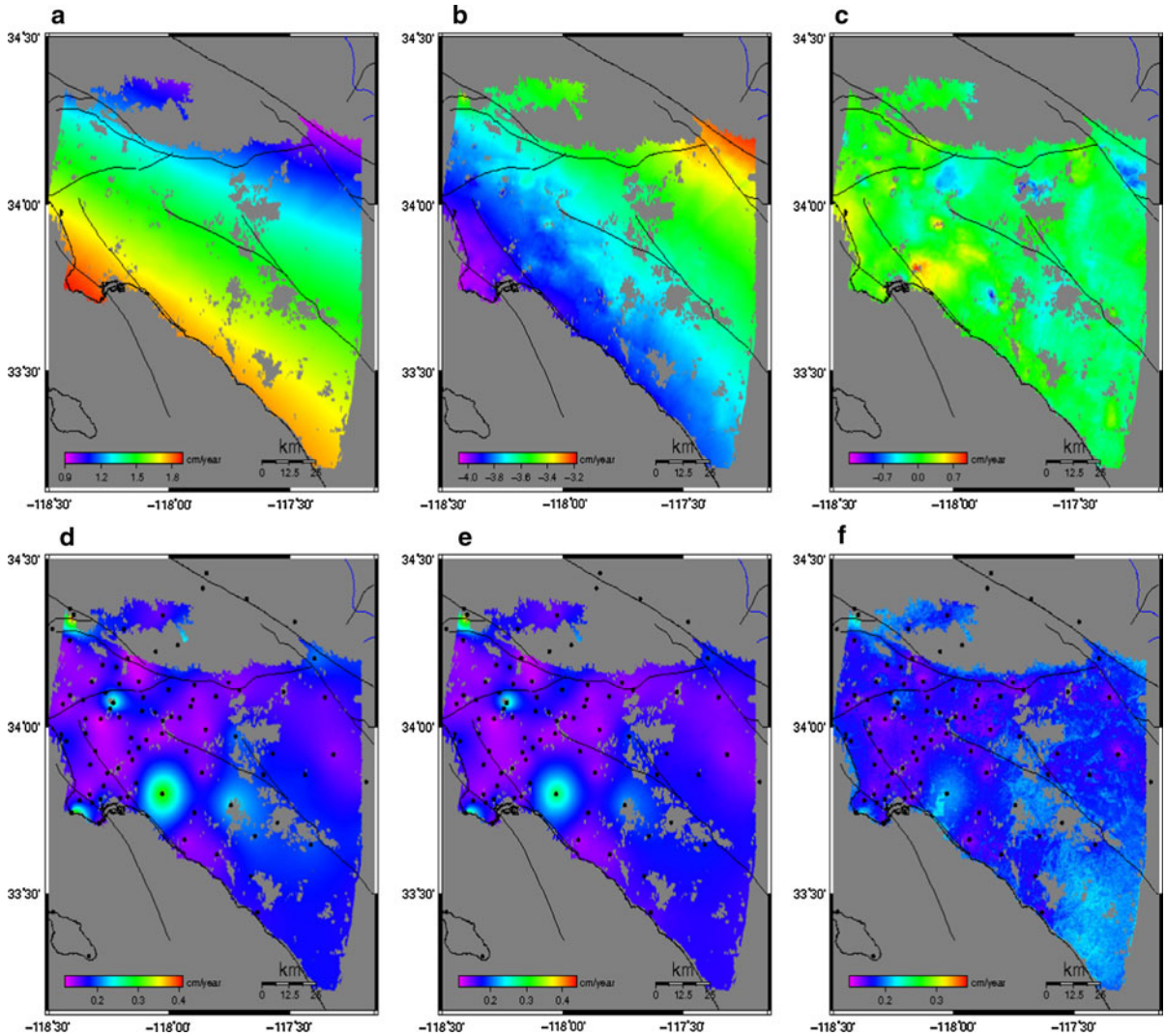

Figure 9
Optimized DInSAR/CGPS images of velocity for the period September 2, 2000 to October 23, 2003: **a** north component, **b** east component, **c** up component, **d** calculated error for the north component, **e** calculated error for the east component, **f** calculated error for the up component

Initial attempts to model the vertical deformation included a genetic algorithm inversion technique, details of which can be found in Tiampo *et al.* (2004), using initial parameter ranges for the aquifer from Poland *et al.* (1109) and Mills *et al.* (1999), and the circular groundwater deformation model from Le Mouélic and Adragna (2002). The depth to the top of the aquifer was fixed at 30 m and Poisson's ratio was set to 0.25. The inversion solved for the head change, *dh*, the radius of the aquifer (*R*), and the center location of the aquifer, *x* and *y*. Results for this inversion are shown in Fig. 11. Note that while the reduced chi-square value for this inversion was ~ 30, the reconstructed model in Fig. 11c does not fit the actual deformation pattern particularly well. This is because the genetic algorithm is attempting to find the best fit solution for a model that does not correspond to pattern particularly well, and therefore is averaging over the remaining points as best as possible. As a result, it significantly underestimates the maximum deformation. In addition, the pattern of horizontal deformation produced by the model does not resemble the actual deformation seen in Fig. 10. The best value for head change is 1.55 cm, while the optimal aquifer radius is 5,977 m.

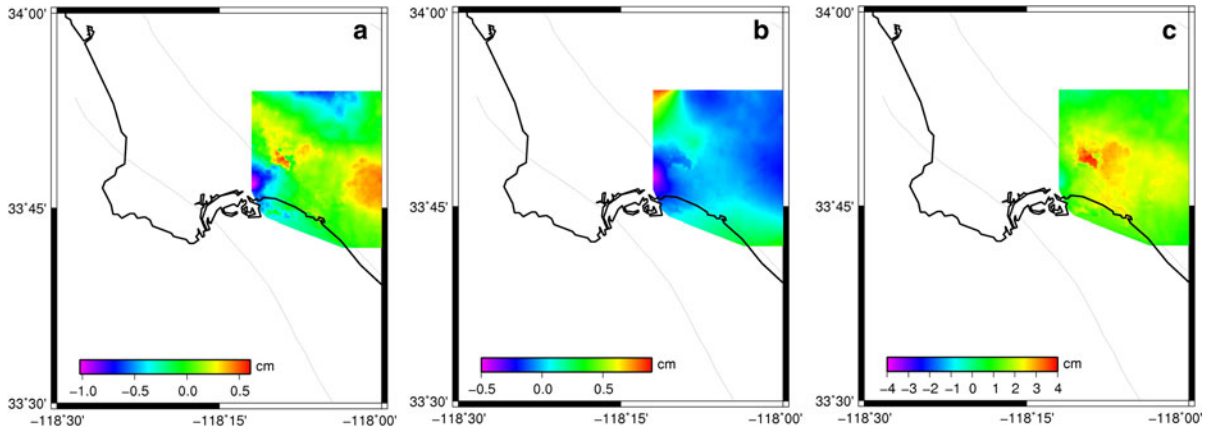

Figure 10
Optimized deformation images for the period September 2, 2000 to October 23, 2003: **a** east component, **b** north component and, **c** up component

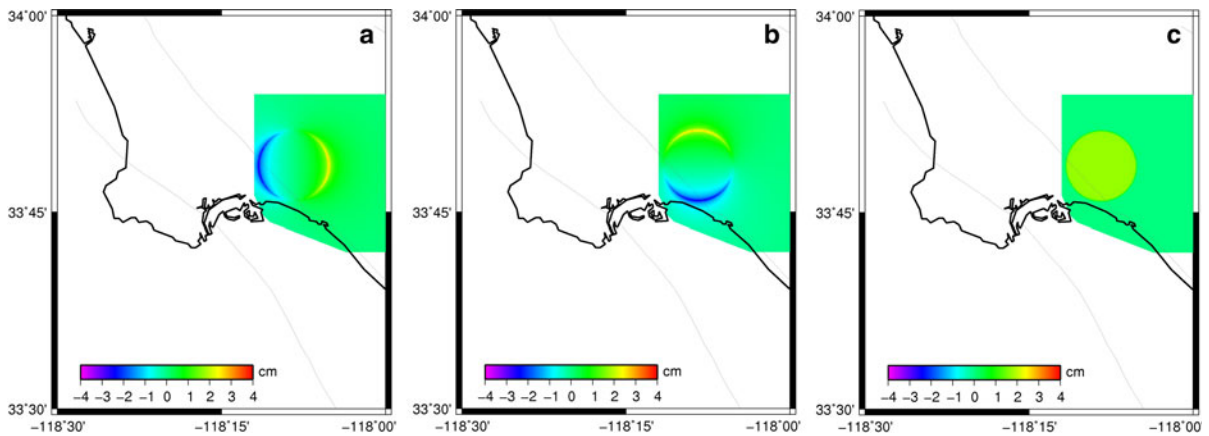

Figure 11
Deformation from circular source of Le Mouélic and Adragna (2002) for **a** east component, **b** north component and **c** up component and the time period September 2, 2000 to October 23, 2003

For comparison, we employed the elliptical deformation model developed above. The same center location was used, with a head change of 1.75 cm and an aquifer radius of 6,000 m, and an eccentricity of 0.5 and a rotation angle of 30° clockwise from horizontal. Results for the vertical deformation are shown in Fig. 12. Here we can see that while this model provides a better fit for the vertical deformation, it still underestimates the maximum uplift. It simplifies the variation in the uplift pattern across the aquifer, and there is a sharp an edge to the deformation at the aquifer edges, without the gradual changes seen by others (Argus *et al.*, 2005). In addition, the horizontal deformation is significantly larger than that of shown in Fig. 10. However, further examination suggests that modeling two separate elliptical sources of varying sizes and pumping volumes, offset and with slightly different rotations, could provide a significantly better fit to both the horizontal and vertical deformation patterns. Further modeling using a more complete inversion technique is necessary to determine the optimal relationship between radius, eccentricity and rotation.

The uplift in this area also differs in sign from that of the long-term regional trends determined by Argus *et al.* (2005). This result is more striking because

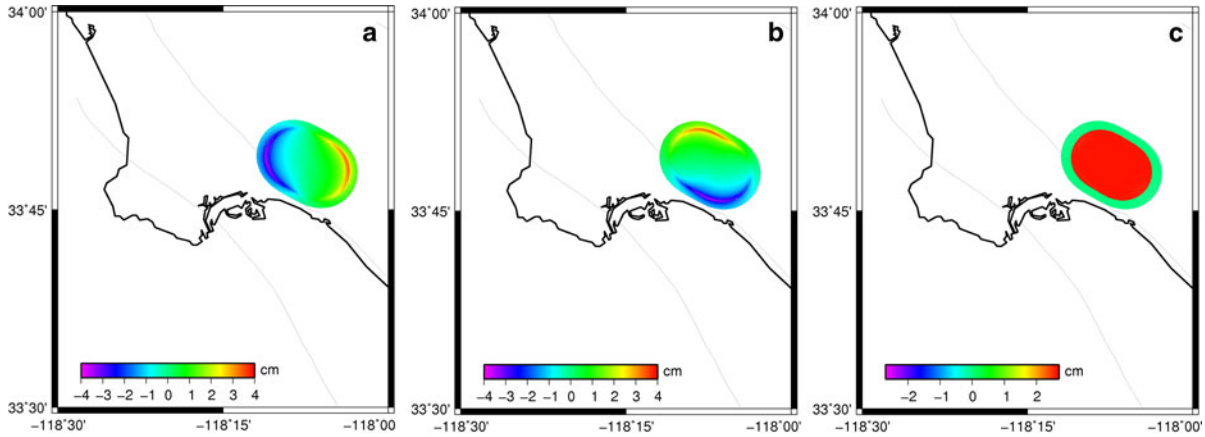

Figure 12
Deformation in the up-direction modeled from the elliptical adaption of the model shown in Fig. 11

other regions of known groundwater subsidence are visible in Fig. 9, in the same sense as observed by others (Watson *et al.*, 2002). Several explanations are possible. The most likely possibility is that temporal fluctuations in the discharge and recharge rates in this particular aquifer region during this particular time period, perhaps coupled with multiple source effects, are modulating the net deformation and obscuring the long-term trend. Further work, including a detailed analysis of many interferograms from this time period and the resulting time series will be necessary to provide a better interpretation.

5. Conclusions

Substantial progress in the detection of land subsidence (and uplift) has been made in recent years with the implementation of modern geodetic techniques, including continuous GPS networks and InSAR (Le Mouélic and Adragna, 2002). Mathematical formulation of the associated surface deformation provides an invaluable technique for the modeling of this deformation and the derivation and analysis of the important constitutive parameters, such as permeability, groundwater height change, and aquifer depth and thickness (Geertsma 1973; Le Mouélic and Adragna, 2002).

In this work we have extended the formula for a circular-shaped reservoir (Geertsma, 1973) to an elliptical-shaped reservoir (Figs. 2, 3, 4) and improved the accuracy of the approximation by making use of the cross terms of the expansion (Figs. 5, 6, 7). Results of the various simulations are encouraging, giving realistic values for the elliptical approximation of the vertical deformation due to groundwater change. It should be noted that, in addition, it is possible to develop a more generic mathematical formulation for an elliptic cylinder using the Mathieu-Hill differential equation and its associated solutions in terms of Mathieu functions (Abramowitz and Stegun, 1970; Valluri *et al.*, 1999, 2005; Vasconcelos *et al.*, 1991). Finally, we have applied the technique to groundwater deformation in southern California and show that model fits the pattern and magnitude of the vertical component of the elliptical signal better than a circular source, although additional studies in other regions that display a clearer elliptical pattern is ongoing in order to establish its universal applicability. The model is generalizable, and further tests will be conducted in order to determine the applicability of the horizontal deformation modeling, including a more detailed inversion for multiple sources.

Acknowledgments

K. F. Tiampo and S. R. Valluri gratefully acknowledge Discovery Grants from National Science Engineering Research Council Canada (NSERC), Human Resources Development Canada (HRDC)

and the UWO Work Study Program for support of F. Ouegnin in this research project. The ERS data were supplied under ESA ENVISAT data grant AO ID = 853 (HAZARDMAP). Technical support for this work has been provided by the POLARIS network. Research by J. Fernández has been supported by Spanish MICINN projects: GEOMOD (CGL2005-05500-C02), PEL2G (CGL2008-06426-C01-01/BTE) and GEOSIR (AYA2010-17448). This research has been partially funded in the frame of the Moncloa Campus of International Excellence (UCM-UPM, CSIC). The DInSAR data was processed by the Repeat Orbit Interferometry Package (ROI PAC) developed at Caltech/Jet Propulsion Laboratory. The DEM data was provided by USGS. The images were plotted with the help of GMT software developed and supported by Paul Wessel and Walter H. F. Smith. The authors would like to thank S. Le Mouélic for providing the original IDL code for the circular deformation model and Dr. D. Argus and Dr. M. Motagh for thorough and helpful reviews.

References

Abramowitz, M. and Stegun, I.A., Handbook of Mathematical Functions (Dover, New York 1970).

Amelung, F., Galloway, D., Bell, J., Zebker, H., and Laczniak, R. (1999), *Sensing the ups and downs of Las Vegas: InSAR reveals structural control of land subsidence and aquifer-system deformation*, Geology *27*, 483-486.

Anderssohn, J., Wetzel, H.U., Walter, T.R., Motagh, M., Djamour, Y., and Kaufmann, H. (2008), *Land subsidence pattern controlled by old alpine basement faults in the Kashmar Valley, northeast Iran: results from InSAR and levelling*. Geophysical Journal International *174*, 287-294.

Argus, D.F., Heflin, M.B., Peltzer, G., Webb, F.H., and Crampe, F. (2005), *Interseismic strain accumulation and anthropogenic motion in metropolitan Los Angeles*, Journal of Geophysical Research *101*, doi:10.1029/2003JB002934.

Argus, D.F., and Gordon, R.G., (2001), *Present tectonic motion across the Coast Ranges and the San Andreas fault system in central California*, Geol. Soc. Am. Bull. *113*, 1580–1592.

Barry, D.A., Parlange, J.Y., Sander, G.C., and Sivaplan, M. (1993), *A class of exact solutions for Richards equation*, J. Hydrology *142*, 29-46.

Bawden, G., Thatcher, W., Stein, R., Hudnut, K., and Peltzer, G., (2001), *Tectonic contraction across Los Angeles after removal of groundwater pumping effects*, Nature *412*, 812-815.

Bell, J.W., Amelung, F., Ferretti, A., Bianchi, M., and Novali, F. (2008), *Permanent scatterer InSAR reveals seasonal and long-term aquifer-system response to groundwater pumping and artificial recharge*. Water Resources Research, *44*, 2 W02407. doi:10.1029/2007WR006152.

Burbey, T.J. (2006), *Three-dimensional deformation and strain induced by municipal pumping, Part 2: Numerical analysis*, J. of Hydrology *330*, 422-434.

Corless, R.M., Gonnet, G.H., Hare, D.E., Jeffrey, D.J., and Knuth, D.E. (1996), *On the Lambert W function*, Adv. Comput. Maths *5*, 329-359.

Dixon, T.H., Amelung, F., Ferretti, A., Novali, F., Rocca, F., Dokka, R., Sella, G., Kim, S.W., Wdowinski, S., and Whitman, D. (2006), *Subsidence and flooding in New Orleans*, Nature *441*, 587-588.

Fernández, J., Romero, R., Carrasco, D., Tiampo, K.F., Rodríguez-Velasco, G., Aparicio, A., Araña, V., and González-Matesan, F.J. (2005), *Detection of displacements in Tenerife Island, Canaries, using radar interferometry*. Geophysical Journal International *160*, 33-45, doi:10.1111/j.1365-246X.2005.02487.x.

Freeze, R.A., and Cherry, J.A., Groundwater (Prentice-Hall, NJ, 1979).

Geertsma, J. (1973), *Land Subsidence above Compacting Oil and Gas Reservoirs*, J. of Petroleum. Tech. *25*, 734-744.

Gourmelen, N., Amelung, F., Francesco, C., Mariarosaria, M., and Lanari, R. (2007), *Mining-related ground deformation in Crescent Valley, Nevada: Implications for sparse GPS networks*, Geophys. Res. Ltrs. *34*, L09309, doi:10.1029/2007GL029427.

Gradshteyn I.S., and Ryzhik, I.M., Table of Integrals Series and Products (Academic Press, NY, 1965).

Hagihara, Y., Celestial Mechanics, v. 1, (MIT Press, 1970).

Hudnut, K., Bock, Y., Galetzka, J., Webb, F., and Young, W. (2002), The Southern California Integrated GPS Network (SCIGN), Seismotectonics in Convergent Plate Boundaries, eds. Y. Fujinawa and A. Yoshgida, Terrapub, 167-189 (http://www.scign.org/).

Jacobs, A., Sandwell, D., Fialko, Y., and Sichoix, L. (2002), *The 1997 (M 7.1) Hector Mine, California, earthquake: Near-field postseismic deformation from ERS interferometry*, Bull. Seis. Soc. Am. *92*, 4, 1433–1442.

King, N.E., Argus, D., Langbein, J., Agnew, D.C., Bawden, G., Dollar, R.S., Liu, Z., Galloway, D., Reichard, E., Yong, A., Webb, F.H., Bock, Y., Stark, K., and Barseghian, D. (2007), *Space geodetic observation of expansion of the San Gabriel Valley, California, aquifer system, during heavy rainfall in winter 2004–2005*, Journal of Geophysical Research *112*, B03409, doi:10.1029/2006JB004448.

Kim, J. (2005), *Three-dimensional numerical simulation of fully coupled groundwater flow and land deformation in unsaturated true anisotropic aquifers due to groundwater pumping*, Water Resources Res., *41*, doi:10.1029/2003WR002941.

Lanari, R., Lundgren, P., Mariarosaria, M., and Casu, F. (2004), *Satellite radar interferometry time series analysis of surface deformation for Los Angeles, California*, Geophys. Res. Ltrs, *31*, L23613, doi:10.1029/2004GL021294, (2004).

Landau L.D., and Lifshitz, E.M. Theory of Elasticity, 3rd edition (Butterworth-Heinemann, Oxford, 1986).

Le Mouélic S., and Adragna, F. (2002), *Ground Uplift in the city of Paris (France) detected by Satellite Radar Interferometry*. Geophys. Res. Letters *29*, 1853, doi:10.1029/2002GL015630.

Li, Z., Muller, J.-P., Cross, P., and Fielding, E.J. (2005), *Interferometric synthetic aperture radar (InSAR) atmospheric correction: GPS, Moderate Resolution Imaging Spectroradiometer (MODIS), and InSAR integration*, J. Geophys. Res. *110*, B03410.

Logsdon, T. Orbital Mechanics: Theory and Applications (Wiley-Interscience, New York, 1997).

Massonnet, D., and Feigl, K.L. (1998), *Radar interferometry and its application to changes in the Earth's surface*, Rev. Geophys., *4*, 441-494.

Massonnet, D., Rossi, M., Carmona, C., Adragna, F., Peltzer, G., and Feigl, K. (1993), *The displacement field of the Landers earthquake mapped by radar interferometry*. Nature *364*, 138–142.

Mills, W., et al. Orange County Water District, Master Plan Report. 371 (Orange County Water District, Fountain Valley, California, 1999).

Motagh, M., Walter, T.R., Sharifi, M.A., Fielding, E., Schenk, A., Anderssohn, J., and Zschau, J. (2008), *Land subsidence in Iran caused by widespread water reservoir overexploitation*, Geophys. Res. Lett. *35*, L16403.

Murray C.D., and Dermott, S.F. Solar System Dynamics (Cambridge University Press, Cambridge, 1999).

Poland, J.F., and Piper, A.M., Ground-water geology of the coastal zone, Long Beach ± Santa Ana area, California, US Geol. Surv. Water-Supply Paper W1109 162 (US Geol. Survey, Reston, Virginia, 1956).

Rosen, P., Hensley, S., Peltzer, G., and Simons, M. (2004), *Updated repeat orbit interferometry package released*, EOS Transactions *85*, 47.

Samsonov, S. and Tiampo, K. (2006), *Analytical optimization of DInSAR and GPS dataset for derivation of three-dimensional surface motion*, Geoscience and remote sensing letters *3*, 107–111.

Samsonov, S., Tiampo, K.F., Rundle, J.B., and Li, Z. (2007), *Application of DInSAR-GPS Optimization for Derivation of Fine-Scale Surface Motion Maps of Southern California*, IEEE Transactions on Geoscience and Remote Sensing *45*, 2, doi: 10.1109/TGRS.2006.887166.

Schmidt, D., and Bürgmann, R. (2003), *Time-dependent land uplift and subsidence in the Santa Clara valley, California, from a large interferometric synthetic aperture radar data set*, Journal of Geophysical Research *108*, doi:10.1029/2002JB002267.

Tesauro, M., Berardino, P., Lanari, R., Sansisti, E., Fornaro, G., and Franschetti, G. (2000), *Urban subsidence inside the city of Napoli (Italy) observed by satellite radar interferometry*, Geophysical Research Letters *27*, 1961-1964.

Tiampo, K.F., Fernández, J., Jentzsch, G., Charco, M., and Rundle, J.B., (2004), *Inverting for the parameters of a volcanic source using a genetic algorithm and a model for magmatic intrusion in elastic-gravitational layered earth models*, Computers and Geosciences *30*, 9, 985-1001.

Tomás, R., Márquez, Y., Lopez-Sanchez, J.M., Delgado, J., Blanco, P., Mallorquí, J.J., Martínez, M., Herrera, G., and Mulas, J. (2005), *Mapping ground subsidence induced by aquifer overexploitation using advanced Differential SAR Interferometry: Vega Media of the Segura River (SE Spain) case study*, Rem. Sens. of Env., *98*, 269-283.

Valluri, S.R., Biggs, R.G., Harper W.L., and Wilson, C. (1999), *The significance of the Mathieu-Hill differential equation for Newton's apsidal precession theorem*, Can. J. Phys. *77*, 393-407.

Valluri, S.R., Chishtie, F.A., and Vajda, A. (2006), *The gravitational wave pulsar signal with Jovian and lunar perturbations and orbital eccentricity corrections*, Class. Quantum. Grav. *23*, 3323-3332.

Valluri, S.R., Jeffrey, D.J., and Corless, R.M. (2000), *Some applications of the Lambert W function to physics*, Can. J. Phys. *78*, 823-831.

Valluri, S.R., Yu, P., Smith, G.E., and Wiegert, P.A. (2005), *An Extension of Newton's Apsidal Precession Theorem*, Mon. Not. R. Astron. Soc. *358*, 1273-1284.

Vasconcelos, E.P., de Oliviera, N.T., and Farias, G.A. (1991), *Surface polaritons on an elliptic cylinder*, Phys Rev B *44*, 24, 13740.

Wang, Z.X., and Guo, D.R. Special Functions (World Scientific, Singapore, 1989).

Watson, K., Bock, Y., and Sandwell, D. (2002), *Satellite interferometric observation of displacements associated with seasonal groundwater in Los Angeles Basin*, J. Geophys. Res. *107*, 2074. doi:10.1029/2001JB000470.

(Received March 1, 2010, revised January 26, 2011, accepted July 10, 2011, Published online September 9, 2011)